

Ab initio velocity-field curves in monoclinic β -Ga₂O₃

Krishnendu Ghosh and Uttam Singiseti

Citation: *Journal of Applied Physics* **122**, 035702 (2017); doi: 10.1063/1.4986174

View online: <http://dx.doi.org/10.1063/1.4986174>

View Table of Contents: <http://aip.scitation.org/toc/jap/122/3>

Published by the *American Institute of Physics*

Articles you may be interested in

[Highly conductive homoepitaxial Si-doped Ga₂O₃ films on \(010\) \$\beta\$ -Ga₂O₃ by pulsed laser deposition](#)

Applied Physics Letters **111**, 012103 (2017); 10.1063/1.4991363

[Modulation-doped \$\beta\$ -\(Al_{0.2}Ga_{0.8}\)₂O₃/Ga₂O₃ field-effect transistor](#)

Applied Physics Letters **111**, 023502 (2017); 10.1063/1.4993569

[A correlation between the defect states and yellow luminescence in AlGa_N/Ga_N heterostructures](#)

Journal of Applied Physics **122**, 035101 (2017); 10.1063/1.4993903

[High reverse breakdown voltage Schottky rectifiers without edge termination on Ga₂O₃](#)

Applied Physics Letters **110**, 192101 (2017); 10.1063/1.4983203

[High responsivity in molecular beam epitaxy grown \$\beta\$ -Ga₂O₃ metal semiconductor metal solar blind deep-UV photodetector](#)

Applied Physics Letters **110**, 221107 (2017); 10.1063/1.4984904

[Improved performance of AlGa_N-based deep ultraviolet light-emitting diodes with nano-patterned Al_N/sapphire substrates](#)

Applied Physics Letters **110**, 191103 (2017); 10.1063/1.4983283

AIP | Journal of
Applied Physics

Save your money for your research.
It's now **FREE** to publish with us -
no page, color or publication charges apply.

Publish your research in the
Journal of Applied Physics
to claim your place in applied
physics history.

Ab initio velocity-field curves in monoclinic β -Ga₂O₃

Krishnendu Ghosh^{a)} and Uttam Singiseti^{b)}

Electrical Engineering Department, University at Buffalo, Buffalo, New York 14260, USA

(Received 2 June 2017; accepted 3 July 2017; published online 19 July 2017)

We investigate the high-field transport in monoclinic β -Ga₂O₃ using a combination of *ab initio* calculations and full band Monte Carlo (FBMC) simulation. Scattering rate calculation and the final state selection in the FBMC simulation use complete wave-vector (both electron and phonon) and crystal direction dependent electron phonon interaction (EPI) elements. We propose and implement a semi-coarse version of the Wannier-Fourier interpolation method [Giustino *et al.*, Phys. Rev. B **76**, 165108 (2007)] for short-range non-polar optical phonon (EPI) elements in order to ease the computational requirement in FBMC simulation. During the interpolation of the EPI, the inverse Fourier sum over the real-space electronic grids is done on a coarse mesh while the unitary rotations are done on a fine mesh. This paper reports the high field transport in monoclinic β -Ga₂O₃ with deep insight into the contribution of electron-phonon interactions and velocity-field characteristics for electric fields ranging up to 450 kV/cm in different crystal directions. A peak velocity of 2×10^7 cm/s is estimated at an electric field of 200 kV/cm. *Published by AIP Publishing.*
[\[http://dx.doi.org/10.1063/1.4986174\]](http://dx.doi.org/10.1063/1.4986174)

I. INTRODUCTION

β -Ga₂O₃ is an emerging wide-bandgap semiconductor with excellent potential for power electronics applications. Experimentally demonstrated high breakdown voltage devices^{1–5} make it an attractive material for next generation power electronics in addition to deep UV optoelectronic applications.^{6,7} However, the low symmetry monoclinic structure and the large primitive cell present immense challenges to accurate prediction of thermal, optical, and electrical transport properties. There have been a number of reports on thermal, dielectric, and optical properties of this material.^{8–15} Recently, we reported low field electron mobility calculation in this material from first principles¹⁶ that fairly agreed with experimental report.¹⁷ However, there is no report on the high field transport properties in this material. High-field electron transport is important not just for electronics but also for several branches of photonics. Electron phonon interactions (EPIs) play an important role in high-field transport. It is important to have a clear quantitative understanding of how EPIs affect high-field electron transport. Traditionally, they are modelled using phenomenological deformation potentials (DPs) that could explain the experimental results. However, such an approach ignores complex issues such as anisotropy and also requires experimental data to set the phenomenological constants. Revealing the right physics of EPI is crucial to engineer the electron and phonon dynamics. In recent years, there have been several studies on calculating phonon scattering rates in GaAs and Si^{18–22} and low field mobilities^{19,22} using EPI from *ab-initio* methods. However, including a full-band *ab-initio* based EPI in a Monte Carlo (MC) algorithm for high transport studies poses several computational challenges especially for materials with many phonon modes. Here, we

systematically study the physics of EPI in β -Ga₂O₃ to reveal how they affect the high-field electron transport calculated using a full band Monte Carlo (FBMC) simulation and also address the computational challenges. Monoclinic β -Ga₂O₃ has a large primitive cell with low crystal symmetry which makes it an ideal benchmark system to study electron transport from first principles. The computational strategy is discussed first followed by the results obtained for β -Ga₂O₃.

II. THEORY AND METHODS

The computation begins with the density functional theory (DFT) calculation on an equilibrium lattice structure followed by the extraction of Kohn-Sham (KS) eigen values. Next, lattice response calculations are done based on the density functional perturbation theory (DFPT).²³ This provides the dynamical phonon matrix and also the perturbation in the self-consistent potential for each perturbation. Diagonalizing the dynamical phonon matrix gives the phonon eigen values. The EPI elements are computed from the perturbation in the self-consistent potential.²³ The EPI elements and the phonon dynamical matrices are interpolated using a Wannier-Fourier interpolation scheme²⁴ to obtain fine sampling of the Brillouin zone. However, the long-range polar optical phonon (POP) EPI needs a separate treatment due to its aperiodic nature. Recent formulation²⁵ on a long-range EPI interpolation scheme is used here.

A. Semi-coarse Electron-Phonon Interaction (EPI) interpolation

The fine resolution needed on both electron (\mathbf{k}) and phonon (\mathbf{q}) wavevector meshes requires large memory in computation which is exacerbated for materials with multiple phonon modes such as β -Ga₂O₃. Unlike scattering rate calculations, an “on the fly” method^{18,26} could not be used in the FBMC calculation since we need to store the EPI matrix

^{a)}kghosh3@buffalo.edu

^{b)}uttamsin@buffalo.edu

elements for final state selection. An “on the fly” calculation inside the final state selection program is inefficient since the summation over the real-space grid has to be performed for each electron, for each time interval, and for each scattering process making it extremely slow. Hence, it is necessary to store the fine grid matrix elements increasing the memory requirement. Here, we propose a semi-coarse Wannier-Fourier interpolation scheme to ease the computational requirement of storing the fine-grid matrix elements. In this method, the unitary rotations are on a fine mesh, but the inverse Fourier transform sum is on a coarse mesh. Storing the fine-grid electron-phonon interaction (EPI) elements requires huge run-time memory. Using the definitions of electronic Wannier functions (WF),²⁴ we write the short range non-polar EPI matrix elements on fine \mathbf{k} and \mathbf{q} meshes as

$$g_{short}^{\nu}(\mathbf{k}, \mathbf{q}) = \frac{1}{N_e^2} U_{\mathbf{k}+\mathbf{q}} \left[\sum_{\mathbf{R}_e, \mathbf{R}'_e} e^{i\mathbf{k} \cdot (\mathbf{R}_e - \mathbf{R}'_e)} g_{short}^{\nu}(\mathbf{R}_e - \mathbf{R}'_e, \mathbf{q}) \right] U_{\mathbf{k}}^{\dagger}. \quad (1)$$

Here, the unitary rotation matrices U have a dimension of $N^w \times N^w$, where N^w is the size of the Wannier subspace. $g_{short}^{\nu}(\mathbf{k}, \mathbf{q})$ is the short-range EPI on both fine meshes. \mathbf{R}_e is the center of a unit cell in the supercell and N_e is the total number of unit cells in the supercell. Eq. (1) shows the inverse Fourier transform of the real-space (on electronic mesh) $g_{short}^{\nu}(\mathbf{R}_e - \mathbf{R}'_e, \mathbf{q})$ to an arbitrary \mathbf{k} -point while the \mathbf{q} -mesh interpolated information is already present on the right-hand side of the equation. The total memory requirement to store the short range EPI on both fine meshes would be governed by $N^k \times N^q \times N^q \times (N^w)^2$, which becomes large for the required N^k and N^q where N^k , N^q , and N^w are the size of the fine k -mesh, q -mesh, and the number of phonon modes, respectively. For this work, the corresponding memory requirement becomes more than 500 terabytes. Hence, we propose a way to circumvent the problem. The primary contribution to $g_{short}^{\nu}(\mathbf{R}_e - \mathbf{R}'_e, \mathbf{q})$ comes when the two involved electronic WFs are on the same unit cell since the overlap of remote WFs is low (although not negligible and we discuss that later) in the case of maximally localized Wannier functions (MLWFs). Under such a condition, we can rewrite (after simple algebraic manipulation) Eq. (1) as

$$g_{short}^{\nu,0}(\mathbf{k}, \mathbf{q}) = \frac{1}{N_e} U_{\mathbf{k}+\mathbf{q}} g_{short}^{\nu}(\mathbf{0}_e, \mathbf{q}) U_{\mathbf{k}}^{\dagger} \\ = U_{\mathbf{k}+\mathbf{q}} U_{\mathbf{k}_c+\mathbf{q}}^{\dagger} g_{short}^{\nu,0}(\mathbf{k} = \mathbf{k}_c, \mathbf{q}) U_{\mathbf{k}_c} U_{\mathbf{k}}^{\dagger}. \quad (2)$$

Hence, the same unit cell contribution $g_{short}^{\nu,0}(\mathbf{k}, \mathbf{q})$ can be accessed just by storing $g_{short}^{\nu,0}(\mathbf{k} = \mathbf{k}_c, \mathbf{q})$ on a coarse \mathbf{k} -mesh (\mathbf{k}_c) and the rotation matrices. This reduces the memory requirement by several orders. Next, we discuss the contribution from remote WFs. Now, we consider Eq. (1) with $\mathbf{R}_e \neq \mathbf{R}'_e$. Under such conditions, a reduction similar to Eq. (2) would have been perfectly possible if the phase factor $e^{i\mathbf{k} \cdot (\mathbf{R}_e - \mathbf{R}'_e)}$ was absent. If the unit cells are far enough from each other (e.g., $\mathbf{R}_e - \mathbf{R}'_e > 5 \times$ lattice spacing), $g_{short}^{\nu}(\mathbf{R}_e - \mathbf{R}'_e, \mathbf{q})$ becomes negligible. However, if

the unit cells are close to each other, because of the \mathbf{k} -space smoothness of the matrix elements in Wannier gauge, the contribution from the remote unit cells is smaller compared to that from the same unit cell. Under such a gauge-choice, treating the remote WF contribution similar to Eq. (2) introduces small inaccuracy in calculation but eases the computational requirement to a great extent. So, the overall $g_{short}^{\nu}(\mathbf{k}, \mathbf{q})$ can be obtained from $g_{short}^{\nu}(\mathbf{k} = \mathbf{k}_c, \mathbf{q})$ and the rotation matrices on the fine mesh. The essential idea is to rotate the coarse-mesh elements to an optimal Bloch-space that produces the maximally localized WF (MLWFs) and perform Fourier transform to real space followed by inverse Fourier transform on another coarse \mathbf{k} -mesh. The fine \mathbf{k} -mesh elements could be obtained “on the fly” just by un-rotating the elements back to the normal Bloch-space using the fine \mathbf{k} -mesh rotation matrices. This reduces the “on the fly” time consumed in converting the elements back and forth between reciprocal and real spaces while at the same time mitigating the huge memory requirement for storing the elements on both fine \mathbf{k} and \mathbf{q} meshes. It is important to mention here that this sacrifice of accuracy does not lead to any sacrifice of the crystal symmetry mediated selection rules of non-polar scattering since that is taken care of inside short range EPI matrix $g_{short}^{\nu}(\mathbf{R}_e - \mathbf{R}'_e, \mathbf{q})$.

B. Full Band Monte Carlo (FBMC) simulation

High-field transport requires Monte Carlo (MC) simulations. The method is widely used for velocity field curves, and we briefly describe the method^{27,28,30,31} here. We solve the Boltzmann transport equation (BTE) using the FBMC technique starting from *ab initio* KS eigen values on a fine reciprocal \mathbf{k} -mesh, phonon eigen values, both long-range (POP) and short range (non-polar) EPIs, and the scattering rates on the fine \mathbf{k} -mesh with contributions from each phonon mode treated separately. For the phonon eigen calculations, we used two different types of \mathbf{q} -meshes: one for short-range elements that span the entire Brillouin zone (BZ), while the other for the long range elements which exist only in the vicinity of the zone center (ZC). Our MC scheme is spatially homogenous, and hence, the spatial gradient term in the BTE disappears. The ensemble of electrons is first initialized in a Maxwellian thermal distribution before the electric field is turned on. Electrons are allowed to drift under the influence of the electric field and to get scattered randomly. The free drifting of the electron changes the crystal momentum according to (in atomic units) $\dot{\mathbf{k}} = \mathbf{F}$, where \mathbf{F} is the applied electric field. The free drifting time (t_0) is estimated²⁸ based on a random number r such that $t_0 = -\frac{1}{\Lambda} \ln r$, where Λ is the maximum possible scattering rate from a given band at any \mathbf{k} point. The final state selection after a scattering mechanism is described next.

The first step of the final state selection process is to identify the mechanism that caused the scattering. A “mechanism” includes the details of phonon mode index, final electronic band index, and the nature (polar/non polar, absorption/emission) of the scattering. So, for 30 phonon modes and 2 electronic bands, the allowed number of mechanisms would be

180. It is noted that polar mechanisms do not contribute to interband scatterings. Finding the scattering mechanism follows from a normalized scattering rate (NSR) table that is formed at each \mathbf{k} point and each band from the previously computed *ab initio* scattering rates. The formation of the NSR table is discussed here briefly. If $S_m^\nu(\mathbf{k})$ denotes the scattering rate of an electron at a wave-vector \mathbf{k} and an initial band m mediated by a mechanism ν , the elements of the NSR table at band m and wave-vector \mathbf{k} have a form

$$NSR(\nu) = \frac{\sum_{i=1}^{\nu} S_m^i(\mathbf{k})}{\max_{\mathbf{k}} \sum_{i=1}^{N_m} S_m^i(\mathbf{k})}. \quad (3)$$

So, the NSR elements always lie in (0, 1) and NSR is non decreasing with increasing ν . The NSR elements are stored in a look-up table whose memory requirement scales as $N^k \times N^b \times N^m$, where N^b is the number of bands taken in the transport calculation and N^m is the total number of scattering mechanisms. The large memory requirement of the NSR in a parallel computing environment is met by storing it on shared memory windows²⁹ available to all processes running under the same computing node. While selecting the mechanism, a random number r' [in (0, 1)] is generated and the mechanism ν is selected if the relation $NSR(\nu) > r > NSR(\nu - 1)$ holds true. If $NSR(N^m) < r$, the electron is “self-scattered,”^{27,28,30,31} which means that the state of the electron remains unchanged.

Given an “actual” scattering event occurs, once the phonon mode, final electronic band, and the nature of the scattering are extracted from the NSR table, the next task is to find the final electronic wave-vector. We use a method tactically similar to the one reported for covalent semiconductors²⁹ and we treat the polar phonon mode scatterings separately. Here, a brief detail of the algorithm is given. Let us consider that the initial electron band index is m and wave-vector is k_i . First, all the \mathbf{k} -points k_j in the final band n that satisfy the energy conservation are shortlisted. Next, a further shortlisting is done based on the strict energy and momentum

conservation with implementation of phonon dispersion. So this gives a list of final k_j points that satisfy both the conservations. Now, we exploit the full-band EPI elements and this is where both \mathbf{k} and \mathbf{q} dependences of the EPI elements are required. Another normalized table (similar to Eq. (3)) is formed based on the product of the local density of states (LDOS) at the potential k_j s and EPI strength at the corresponding momentum conserving phonon wave-vector, q_j . This is where the polar scattering needs to be taken care of separately. The small-angle preference of the polar mechanisms needs to be properly captured in order to reflect the lower momentum relaxation time compared to corresponding energy relaxation time. This is done with the aid of a separate fine \mathbf{q} -mesh that exists only near the zone center. Using a random number, the normalized table is scanned through like it was done for NSR and a final k_j is selected. However, this only gives the grid point in the reciprocal space. The final electron wave-vector could belong to anywhere within the small cube that is represented by this grid point. The scheme to select the final wave-vector within the small cube is exactly the same as the one described in steps (e)–(g) of Fig. 7 in Ref. 29. Next, we discuss the calculation and results for β -Ga₂O₃.

III. RESULTS AND DISCUSSION

We carry out DFT calculations on β -Ga₂O₃ as described in our previous work¹⁶ with similar pseudo-potentials³⁵ and zone sampling³⁶ using Quantum ESPRESSO.³⁷ Figure 1(a) shows the crystal structure of β -Ga₂O₃ along with the Cartesian direction convention that is followed throughout this work. In Fig. 1(b), we show the resulting KS eigen values along two reciprocal vectors. Four conduction bands are shown out of which the first two are used in subsequent transport calculations. Figure 1(c) shows the equi-energy surfaces for two different energies. It can be seen that at a lower energy the surface is spherically symmetric, while at higher energies the surface becomes anisotropic with contributions from higher energy bands. We interpolated the KS Hamiltonian through MLWFs by using the wannier90

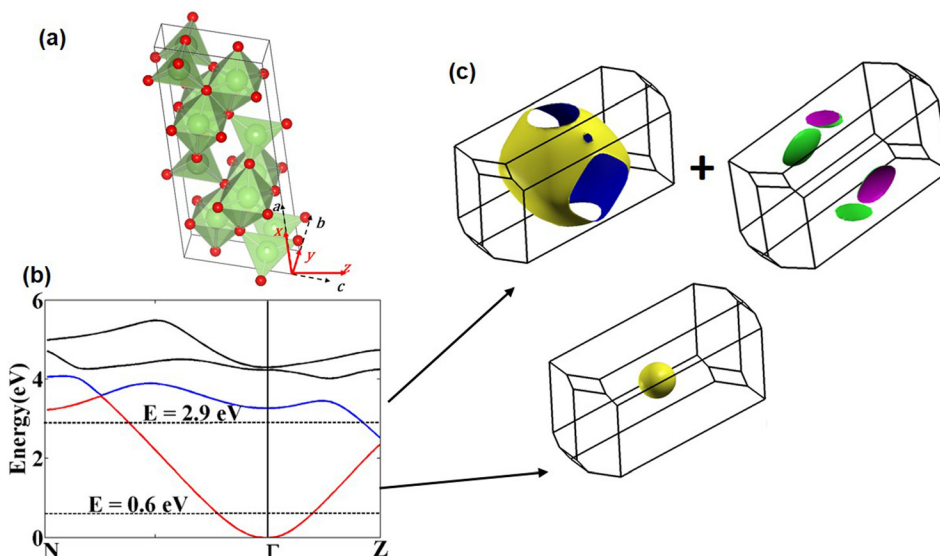


FIG. 1. (a) Crystal structure of β -Ga₂O₃. a , b , and c represent the conventional lattice directions for monoclinic crystals. The Cartesian x , y , and z directions used for the calculations are also shown. (b) The DFT calculated conduction band energies are shown for β -Ga₂O₃. The first two bands (shown in red and blue) are used in the transport calculation. (c) The equi-energy surfaces are shown for two different energies. It is evident that at lower energy the surface is spherically symmetric while higher energy introduces band anisotropy and also multiple bands. (a) is visualized by Vesta^{32,33} and (c) is visualized by XcrySDen.³⁴

code.³⁸ Our optimal Wannier subspace (S) consists of two low lying conduction bands within a frozen energy window. The phonon calculation is done under DFPT using QE. The phonon eigen values and the short-range (non-polar) EPI matrix elements are interpolated on a fine \mathbf{q} -mesh using a modified version of the EPW code.²⁶

A. EPI in β -Ga₂O₃

The short-range non-polar EPI elements are primarily responsible for higher momentum and energy relaxation rates at high-fields that lead to saturation in velocity. The Wannier-Fourier interpolated short-range matrix elements are shown in Fig. 2(a) with respect to \mathbf{q} . We show the sum of the squared magnitude of the coupling over all the vibrational modes. The long-range POP coupling is also shown on the same plot for comparison. The \mathbf{q} dependence of EPI matrix elements ($\sum_v |g_{short}^v|^2$) is to be noted along with its crystal direction dependence (Γ -Z and Γ -N), and the strength is minimized at the Γ point. The inset shows a contour plot on the 2D plane formed by the same two directions. The symmetry of the short-range element observed on the contour plot is a signature of the inversion symmetry associated with the C_{2m} space group.³⁹ The small discontinuity on the short-range EPI marked by the arrow is a result of the gauge ambiguity arising from degenerate final electronic states [see Fig. 1(b)]. Such discontinuity does not affect the total scattering rate since the latter is gauge-invariant. Figure 2(b) shows the short-range EPI for each phonon mode for two different \mathbf{q} vectors. The red bars show $|g_{short}^v|^2$ for initial electron wave-vector \mathbf{k} at $0.25 \times \Gamma Z$ away from Γ while the phonon wave-vector (\mathbf{q}) is $0.5 \times \Gamma Z$ away from Γ . The corresponding two points from the green bars are $0.125 \times \Gamma N$ (\mathbf{k}) away from Γ and $0.25 \times \Gamma N$ (\mathbf{q}) away from Γ . The inset of Fig. 2(b) shows the scattering schematic for high energy electrons. The long arrows correspond to a direction reversal of an electron which provides a high momentum relaxation. For high-field transport, the available phase space allows phonon wave-vectors from all directions. But the higher momentum relaxing phonon wave-vectors need to be inclined as much opposite as possible to the propagating

electron wave-vector. This explains the choice of electron and phonon wave-vectors to show the individual mode contributions in Fig. 2(b). It could be seen that for an electron with initial wave-vector at the Γ point, the dominating non-polar phonon modes are at 83 and 96 meV along Γ -Z, while along Γ -N, they are 22 and 90 meV. Figure 2(c) shows the short range EPI element ($g_{short}^v(\mathbf{k})$) along the Γ -Z- Γ direction calculated using the coarse mesh, fine mesh, and semi-coarse sampling proposed in this work. The \mathbf{q} vector for these calculations is kept fixed at halfway along the ΓZ . The DFPT calculated coarse-mesh element is shown with red dots, while a regular fine mesh interpolated result is shown with a red solid curve. The kinks on the semi-coarse curves occur when the representative coarse \mathbf{k} -mesh point corresponding to a fine- \mathbf{k} mesh point changes. The small errors incurred due to this strategy are acceptable given the resulting ease in computational memory requirement. The key aspect is that the coarse mesh used in the Fourier transform does not have to be as coarse as the original DFT mesh. It should be made as fine as possible within the available computational resources. The maximum observed deviation between the $8 \times 8 \times 4$ semi-coarse mesh and the fine mesh elements is $\sim 12\%$ along the Γ -Z- Γ direction for this given \mathbf{q} vector.

B. Scattering rates and high-field transport

Next, we discuss the Fermi-Golden rule computed non-polar phonon scattering rates. The energy conserving delta function is implemented using a Lorentzian smearing. We carried out an analytical fitting of the computed scattering rates using a deformation potential (DP) approximation³¹ to guide future analytical transport calculations. However, it is important to note that resulting fitting parameters do not provide any actual physical picture of EPI or existence of phonon modes. The density of states used in the scattering rate fitting procedure is computed from the *ab initio* bandstructure. For non-polar optical phonon scattering [Fig. 3(a)], we fitted the computed scattering rates with $D_0^2/\omega_0 = 7.2 \times 10^{18}$ eV/cm², where D_0 is the optical deformation potential and ω_0 is the optical phonon energy. For a suitable fitting, these two parameters are inter-adjustable and hence are not

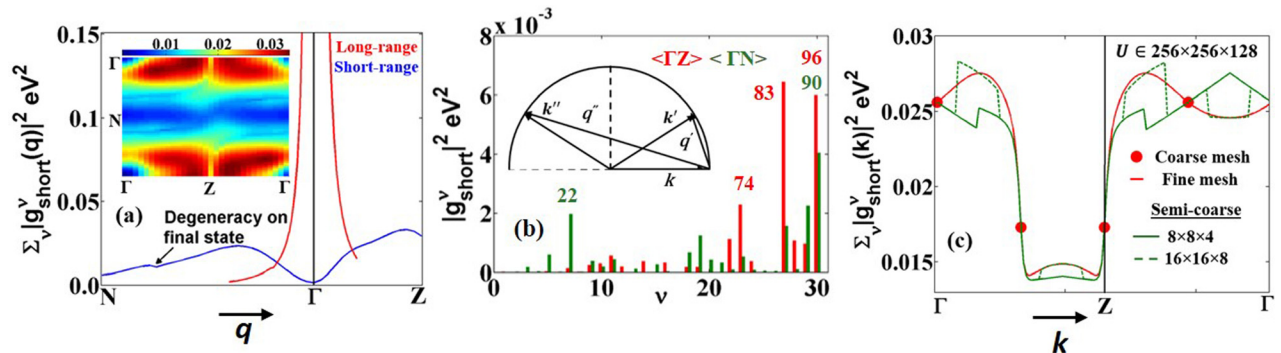


FIG. 2. (a) The dependence of the EPI elements with the phonon wave-vector (\mathbf{q}). The inset shows a contour plot of the short-range EPI on the ΓZ - ΓN plane. The initial electronic state is taken at the Γ , and hence, the inversion symmetry of the crystal is reflected in the contour plot. (b) The mode-wise splitting of the short-range EPI for two \mathbf{q} points along two different directions. The phonon energies (meV) for the dominating modes are shown with corresponding colors. (Inset) At higher electron energies, a high momentum relaxation requires phonon wave-vectors that are inclined towards the opposite direction of the electronic wave-vector. (c) The interpolated elements in \mathbf{k} -space using the semi-coarse \mathbf{k} -mesh strategy. The \mathbf{q} point is kept fixed at a point halfway along ΓZ . A pure fine-mesh interpolation is also shown for comparison. In (a)–(c), the initial and final electronic band indices are taken to be the first band.

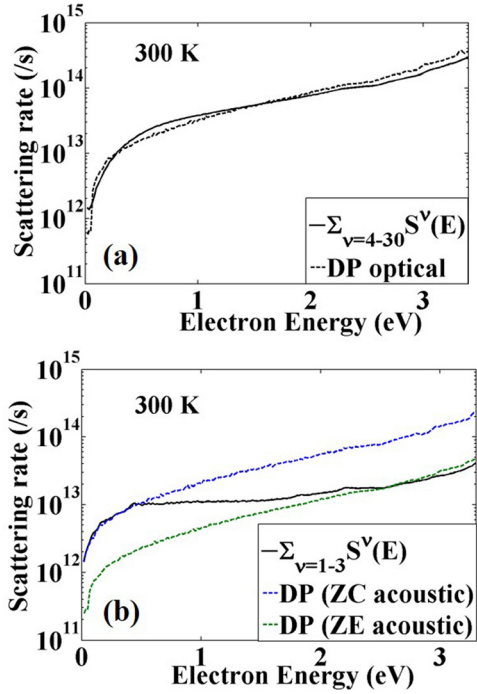


FIG. 3. (a) Comparison of computed non-polar optical phonon (NOP) scattering rate and fitted NOP scattering rate. (b) Comparison of computed acoustic phonon scattering rate with the corresponding fittings. The fitting splits the contribution from zone-center and zone edge acoustic modes. See text for fitting parameters.

unique. Figure 3(a) shows the fitted curves with dashed curves. Figure 3(b) shows the calculated acoustic phonon scattering rate with energy. For acoustic phonons, the fitting procedure is two-fold as seen in Fig. 3(b). Scattering due to the zone-center (ZC) phonons is fitted with $D_A^2/v_s^2 = 5 \times 10^{-11} \text{ eV}^2 \text{ s}^2/\text{cm}^2$, where D_A is the acoustic deformation potential and v_s is the velocity of sound. On the other hand, the zone-edge (ZE) acoustic phonons have a dispersion similar to optical phonons; hence, we use an optical phonon like fitting with $D_{AZE} = 5 \times 10^7 \text{ eV/cm}$ and $\omega_{AZE} = 0.01 \text{ eV}$

[dashed green lines in Fig. 3(b)]. A single fitting of the acoustic scattering rate is not possible because of the approximations³¹ used to derive the analytical form of the scattering rate, namely, the negligible phonon energy and the linear dependence of the coupling with phonon wave-vector.

Now, we discuss the results of the Monte Carlo simulation. Figure 4(a) shows the initialized Maxwell electron distribution in energy space at room temperature at the start of the FBMC simulation, while Fig. 4(b) shows the initial electron distribution along k_z in the direction (z -direction) of the applied electric field. The respective bottom panels [Figs. 4(c) and 4(d)] show similar plots for an applied electric field of 300 kV/cm along the z direction. It is noted that the non-equilibrium distribution in energy space dies off well beyond 2 eV of energy. The first satellite valley occurs at $\sim 2.5 \text{ eV}$; hence, very few electrons are transferred to satellite valleys at the field strength. This is further supported by the electron distribution as a function of k_z seen in Fig. 4(d), which shows very low population near the zone edge where the valley occurs. Next, we discuss the transient response of the drift velocity as shown in Fig. 5. At low electric fields, the transport is dominated by POP scattering and the momentum relaxation rate is not increasing with electron energy implying that the drift velocity monotonically arrives to a steady state. However, beyond 150 kV/cm velocity, overshoot starts to appear. This is attributed to the fact that with increasing electron energy, the intra-band non-polar scattering becomes significantly high allowing short-range transitions that boost up momentum relaxation drastically while the energy relaxation is still limited by the energy of the phonon modes. The imbalance of the two rates results³¹ in a slow rise of the electron energy than the same in the drift velocity. However, the momentum relaxation rate is also dependent on the electron energy and hence it gets adjusted in a larger time-scale than that of the drift velocity and hence we see the overshoot.

Figure 6 shows the velocity-field curves in three different Cartesian directions calculated from FBMC using the

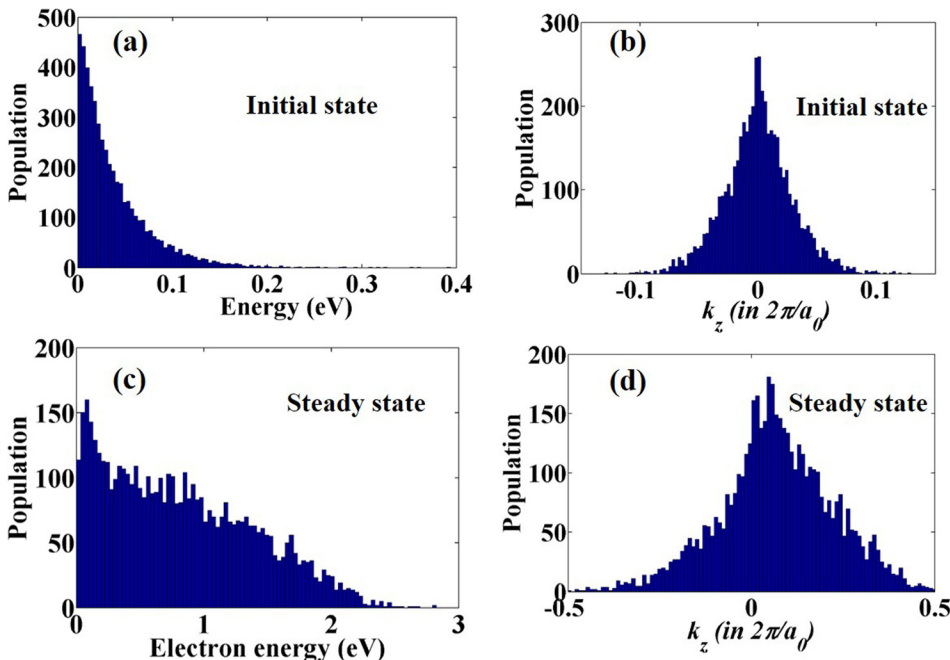


FIG. 4. Electron population in energy space and k_z space. (a) and (b) show the histogram plots for initial conditions used in the FBMC simulation and (c) and (d) show the corresponding plots for the steady state under an external electric field of 300 kV/cm applied along the z direction.

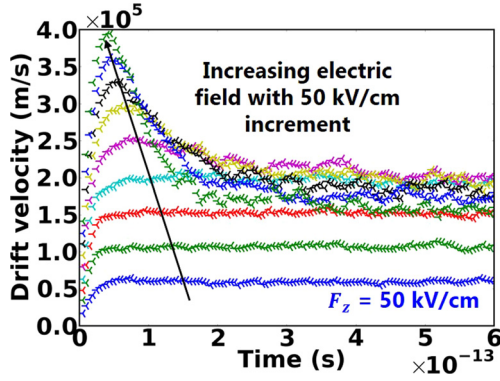


FIG. 5. Transient response of drift velocity for different electric fields.

scattering strengths discussed in Secs. II and III A. We see that the velocity increases in all three directions up to 200 kV/cm followed by a negative differential conductivity (NDC). The calculated NDC is less than that observed in GaAs since the satellite valleys occur at a much higher energy (the lowest one being at ≈ 2.4 eV) as compared to GaAs (≈ 0.3 eV). Unlike GaAs and GaN where the NDC results from inter-valley scattering, the NDC and velocity saturation in β -Ga₂O₃ result from intra-valley short-range scattering. In β -Ga₂O₃, the non-parabolic nature of the Γ valley at higher electronic energies reduces the average electronic group velocities resulting in the NDC and the short range intra-valley EPI results in the saturation of velocity. For the range of electric fields considered here, electrons barely reach the satellite valleys [see Fig. 4(c)]. So, the fact that the velocity starts rolling off from its peak value beyond 200 kV/cm is to be attributed to the non-parabolicity of the conduction band rather than intervalley scatterings. The average peak velocity at an electric field of 200 kV/cm is $\approx 2 \times 10^7$ cm/s which is slightly lower than that of wurtzite GaN.⁴⁰ Next, we discuss the observed anisotropy in the velocity-field curves. Prior to the peak velocity point, around 100 kV/cm, the z direction velocity is lower than that in x and y directions. This is attributed to the large polar optical phonon scattering by the B_u^1 mode which is polarized in the z direction as was observed in our previous work.¹⁶ More details on this anisotropy could be found in a future work.⁴¹ However, beyond the peak velocity, the drift velocity is relatively higher in the y direction. We attribute this to the fact

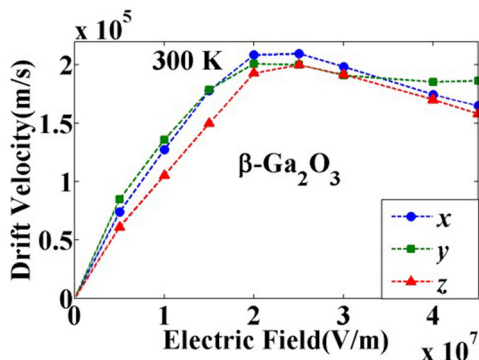
FIG. 6. Velocity-field characteristic of β -Ga₂O₃ at room temperature in three different directions.

TABLE I. Analytical fitting parameters for the computed velocity-field curves.

	x	y	z
μ_0 (cm ² /V s)	140	140	112
v_{sat} (cm/s)	10^7	1.5×10^7	10^7
F_c (V/cm)	2.25×10^5	1.54×10^5	2.63×10^5
γ	2.84	2.47	3.35

that the slope of the energy band drops at a higher \mathbf{k} in the y direction compared to that in the other two directions. Hence, the ensemble average of the drift velocity is higher in the y direction. The velocity-field curves were fitted using the Barnes model⁴² that formulates NDC with, $\mu_n(F) = \frac{\mu_0 + \frac{v_{sat}}{F} (\frac{F}{F_c})^\gamma}{1 + (\frac{F}{F_c})^\gamma}$, where μ_0 is the low-field mobility and v_{sat} , F_c , and γ are the adjustable fitting parameters. This model is used in commercial device simulators⁴³ to simulate device operation. The fitting parameters in three different directions are given in Table I. It is noted that, these parameters are good only up to an electric field of about 500 kV/cm. Beyond that, other physical phenomena such as interband transitions and impact ionization are likely to kick in which will modify the velocity-field curves.

IV. SUMMARY

In summary, we have highlighted the role of full-band EPI in controlling the electron transport in β -Ga₂O₃. A semi-coarse \mathbf{k} -mesh version of the Wannier-Fourier interpolation²⁴ strategy is proposed for the short-range EPI in order to make it computationally tractable in a Monte Carlo algorithm. The applicability of this strategy is valid within the current scope of this work; however, for validating this method for arbitrary material systems, further study is required which itself could be a topic for future work. The calculated EPIs are used in an FBMC algorithm to analyze high-field transport. Scattering rate fitting parameters are calculated to guide analytical calculations. Monoclinic β -Ga₂O₃ is studied under this theoretical manifold followed by the prediction of the velocity-field characteristics. The velocity-field curves are fitted in different directions using compact NDC models to guide device design.

ACKNOWLEDGMENTS

The authors acknowledge the support from the National Science Foundation (NSF) Grant (No. ECCS 1607833). The authors also acknowledge the excellent high performance computing cluster provided by the Center for Computational Research (CCR) at the University at Buffalo.

¹M. Higashiwaki, K. Sasaki, T. Kamimura, M. Hoi Wong, D. Krishnamurthy, A. Kuramata, T. Masui, and S. Yamakoshi, "Depletion-mode Ga₂O₃ metal-oxide-semiconductor field-effect transistors on β -Ga₂O₃ (010) substrates and temperature dependence of their device characteristics," *Appl. Phys. Lett.* **103**(12), 123511 (2013).

²M. Higashiwaki, K. Sasaki, A. Kuramata, T. Masui, and S. Yamakoshi, "Gallium oxide (Ga₂O₃) metal-semiconductor field-effect transistors on single-crystal β -Ga₂O₃ (010) substrates," *Appl. Phys. Lett.* **100**(1), 013504 (2012).

- ³T. Oishi, Y. Koga, K. Harada, and M. Kasu, "High-mobility β -Ga₂O₃ 201 single crystals grown by edge-defined film-fed growth method and their Schottky barrier diodes with Ni contact," *Appl. Phys. Express* **8**(3), 031101 (2015).
- ⁴K. Sasaki, M. Higashiwaki, A. Kuramata, T. Masui, and S. Yamakoshi, "Schottky barrier diodes fabricated by using single-crystal β -Ga₂O₃ (010) substrates," *IEEE Electron Device Lett.* **34**(4), 493–495 (2013).
- ⁵K. Zeng, K. Sasaki, A. Kuramata, T. Masui, and U. Singiseti, "Depletion and enhancement mode β -Ga₂O₃ MOSFETs with ALD SiO₂ gate and near 400 V breakdown voltage," in *74th Annual Device Research Conference (DRC)* (IEEE, 2016), pp. 1–2.
- ⁶S. Nakagomi, T. Momo, S. Takahashi, and Y. Kokubun, "Deep ultraviolet photodiodes based on β -Ga₂O₃/SiC heterojunction," *Appl. Phys. Lett.* **103**(7), 072105 (2013).
- ⁷T. Oshima, T. Okuno, N. Arai, N. Suzuki, S. Ohira, and S. Fujita, "Vertical solar-blind deep-ultraviolet Schottky photodetectors based on β -Ga₂O₃ substrates," *Appl. Phys. Express* **1**(1), 011202 (2008).
- ⁸B. Liu, M. Gu, and X. Liu, "Lattice dynamical, dielectric, and thermodynamic properties of β -Ga₂O₃ from first principles," *Appl. Phys. Lett.* **91**(17), 172102 (2007).
- ⁹Z. Guo, A. Verma, X. Wu, F. Sun, A. Hickman, T. Masui, A. Kuramata, M. Higashiwaki, D. Jena, and T. Luo, "Anisotropic thermal conductivity in single crystal β -gallium oxide," *Appl. Phys. Lett.* **106**(11), 111909 (2015).
- ¹⁰M. Schubert, R. Korlacki, S. Knight, T. Hofmann, S. Schöche, V. Darachieva, E. Janz_en, B. Monemar, D. Gogova, Q. T. Thieu, R. Togashi, H. Murakami, Y. Kumagai, K. Goto, A. Kuramata, S. Yamakoshi, and M. Higashiwaki, "Anisotropy, phonon modes, and free charge carrier parameters in monoclinic β -gallium oxide single crystals," *Phys. Rev. B* **93**(12), 125209 (2016).
- ¹¹Y. Zhang, J. Yan, G. Zhao, and W. Xie, "First-principles study on electronic structure and optical properties of Sn-doped β -Ga₂O₃," *Phys. B: Condens. Matter* **405**(18), 3899–3903 (2010).
- ¹²S. Badescu, D. Thomson, J. Mann, and G. Jessen, "Atomistic modelling for predicting β -Ga₂O₃ properties," paper presented at the 1st International Workshop on Gallium Oxide and Related Materials, Kyoto University, Kyoto, Japan (2015).
- ¹³M. Schubert, "Coordinate-invariant Lyddane-Sachs-Teller relationship for polar vibrations in materials with monoclinic and triclinic crystal systems," *Phys. Rev. Lett.* **117**(21), 215502 (2016).
- ¹⁴F. Ricci, F. Boschi, A. Baraldi, A. Filippetti, M. Higashiwaki, A. Kuramata, V. Fiorentini, and R. Fornari, "Theoretical and experimental investigation of optical absorption anisotropy in β -Ga₂O₃," *J. Phys.: Condens. Matter* **28**(22), 224005 (2016).
- ¹⁵K. A. Mengle, G. Shi, D. Bayerl, and E. Kioupakis, "First-principles calculations of the near-edge optical properties of β -Ga₂O₃," *Appl. Phys. Lett.* **109**(21), 212104 (2016).
- ¹⁶K. Ghosh and U. Singiseti, "Ab initio calculation of electron-phonon coupling in monoclinic β -Ga₂O₃ crystal," *Appl. Phys. Lett.* **109**(7), 072102 (2016).
- ¹⁷A. Parisini and R. Fornari, "Analysis of the scattering mechanisms controlling electron mobility in β -Ga₂O₃ crystals," *Semicond. Sci. Technol.* **31**(3), 035023 (2016).
- ¹⁸M. Bernardi, D. Vigil-Fowler, C. S. Ong, J. B. Neaton, and S. G. Louie, "Ab initio study of hot electrons in GaAs," *Proc. Natl. Acad. Sci. U. S. A.* **112**(17), 5291–5296 (2015).
- ¹⁹J.-J. Zhou and M. Bernardi, "Ab initio electron mobility and polar phonon scattering in GaAs," *Phys. Rev. B* **94**(20), 201201 (2016).
- ²⁰M. Bernardi, D. Vigil-Fowler, J. Lischner, J. B. Neaton, and S. G. Louie, "Ab initio study of hot carriers in the first picosecond after sunlight absorption in silicon," *Phys. Rev. Lett.* **112**(25), 257402 (2014).
- ²¹J. Zhou, B. Liao, and G. Chen, "First-principles calculations of thermal, electrical, and thermoelectric transport properties of semiconductors," *Semicond. Sci. Technol.* **31**(4), 043001 (2016).
- ²²J. Sjakste, N. Vast, M. Calandra, and F. Mauri, "Wannier interpolation of the electron phonon matrix elements in polar semiconductors: Polar-optical coupling in GaAs," *Phys. Rev. B* **92**, 054307 (2015).
- ²³A. D. C. S. Baroni and S. De. Gironcoli, "Phonons and related crystal properties from density-functional perturbation theory," *Rev. Mod. Phys.* **73**, 515–562 (2001).
- ²⁴F. Giustino, M. L. Cohen, and S. G. Louie, "Electron-phonon interaction using Wannier functions," *Phys. Rev. B* **76**(16), 165108 (2007).
- ²⁵C. Verdi and F. Giustino, "Frohlich electron-phonon vertex from first principles," *Phys. Rev. Lett.* **115**(17), 176401 (2015).
- ²⁶J. Noffsinger, F. Giustino, B. D. Malone, C.-H. Park, S. G. Louie, and M. L. Cohen, "EPW: A program for calculating the electron-phonon coupling using maximally localized Wannier functions," *Comput. Phys. Commun.* **181**(12), 2140–2148 (2010).
- ²⁷D. Vasilevka and S. M. Goodnick, see <https://nanohub.org/resources/9109> for Bulk Monte Carlo: Implementation details and source codes download, 2010.
- ²⁸C. Jacoboni and L. Reggiani, "The Monte Carlo method for the solution of charge transport in semiconductors with applications to covalent materials," *Rev. Mod. Phys.* **55**(3), 645 (1983).
- ²⁹MPI: A message-passing interface standard version 3.0, 2012.
- ³⁰T. Kunikiyo, M. Takenaka, Y. Kamakura, M. Yamaji, H. Mizuno, M. Morifuji, K. Taniguchi, and C. Hamaguchi, "A Monte Carlo simulation of anisotropic electron transport in silicon including full band structure and anisotropic impact-ionization model," *J. Appl. Phys.* **75**(1), 297 (1994).
- ³¹M. Lundstrom, *Fundamentals of Carrier Transport* (Cambridge University Press, 2009).
- ³²K. Momma and F. Izumi, "VESTA: A three-dimensional visualization system for electronic and structural analysis," *J. Appl. Crystallogr.* **41**(3), 653–658 (2008).
- ³³See <http://www.misasa.okayama-u.ac.jp/~masami/vesta/Ga2O3-beta-vesta> for the cif file for β -Ga₂O₃.
- ³⁴A. Kokalj, "Computer graphics and graphical user interfaces as tools in simulations of matter at the atomic scale," *Comput. Mater. Sci.* **28**(2), 155–168 (2003).
- ³⁵J. P. Perdew and Y. Wang, "Accurate and simple analytic representation of the electron gas correlation energy," *Phys. Rev. B* **45**(23), 13244–13249 (1992).
- ³⁶H. J. Monkhorst and J. D. Pack, "Special points for Brillouin-zone integrations," *Phys. Rev. B* **13**(12), 5188–5192 (1976).
- ³⁷P. Giannozzi, S. Baroni, N. Bonini, M. Calandra, R. Car, C. Cavazzoni, D. Ceresoli, G. L. Chiarotti, M. Cococcioni, I. Dabo, A. Dal Corso, S. de Gironcoli, S. Fabris, G. Fratesi, R. Gebauer, U. Gerstmann, C. Gougoussis, A. Kokalj, M. Lazzeri, L. Martin-Samos, N. Marzari, F. Mauri, R. Mazzarello, S. Paolini, A. Pasquarello, L. Paulatto, C. Sbraccia, S. Scandolo, G. Sclauzero, A. P. Seitsonen, A. Smogunov, P. Umari, and R. M. Wentzcovitch, "Quantum espresso: A modular and open-source software project for quantum simulations of materials," *J. Phys. Condens. Matter* **21**(39), 395502 (2009).
- ³⁸A. A. Mosto_, J. R. Yates, Y.-S. Lee, I. Souza, D. Vanderbilt, and N. Marzari, "Wannier90: A tool for obtaining maximally localised Wannier functions," *Comput. Phys. Commun.* **178**(9), 685–699 (2008).
- ³⁹See <http://homepage.univie.ac.at/nikos.pinotsis/spacegroup.html#12> for the 4 symmetry operations are identity, inversion, 2-fold rotation around the unique axis, and a mirror symmetry across the plane perpendicular to the unique axis.
- ⁴⁰J. Kolnik, I. H. O. Guzman, K. F. Brennan, R. Wang, P. P. Ruden, and Y. Wang, "Electronic transport studies of bulk zincblende and wurtzite phases of GaN based on an ensemble Monte Carlo calculation including a full zone band structure," *J. Appl. Phys.* **78**(2), 1033–1038 (1995).
- ⁴¹K. Ghosh and U. Singiseti, "Anisotropy of electron transport in monoclinic β -Ga₂O₃ crystal" (unpublished).
- ⁴²J. J. Barnes, R. J. Lomax, and G. I. Haddad, "Finite-element simulation of GaAs MESFET's with lateral doping profiles and submicron gates," *IEEE Trans. Electron Devices* **23**(9), 1042–1048 (1976).
- ⁴³Atlas, Device Simulator. "Atlas user's manual." Silvaco International Software, Santa Clara, CA, USA (2016).